Revealing the mechanical and microstructural performance of multiphase steels during tensile, forming and flanging operations

Efthymiadis, P, Hazra, S, Clough, A, Lakshmi, R, Alamoudi, A, Dashwood, R & Shollock, B

Original citation:
Efthymiadis, P, Hazra, S, Clough, A, Lakshmi, R, Alamoudi, A, Dashwood, R & Shollock, B 2017, 'Revealing the mechanical and microstructural performance of multiphase steels during tensile, forming and flanging operations' *Materials Science and Engineering A*, vol 701, pp. 174-186
https://dx.doi.org/10.1016/j.msea.2017.06.056

DOI 10.1016/j.msea.2017.06.056
ISSN 0921-5093

Publisher: Elsevier

Materials Science & Engineering A 701 (2017) 174–186

Contents lists available at ScienceDirect

Materials Science & Engineering A

journal homepage: www.elsevier.com/locate/msea

Revealing the mechanical and microstructural performance of multiphase steels during tensile, forming and flanging operations

P. Efthymiadis[a,*], S. Hazra[a], A. Clough[a], R. Lakshmi[a], A. Alamoudi[a], R. Dashwood[b], B. Shollock[a]

[a] WMG, Warwick University, Coventry CV4 7AL, UK
[b] Vice Chancellor's Office, Coventry University, Coventry CV4 7AL, UK

ARTICLE INFO

Keywords:
Ultra high strength steels
Formability
Flanging
Springback
Microstructure properties-mechanical performance correlation

ABSTRACT

The mechanical performance of Dual Phase (DP) and Complex Phase (CP) steels was investigated by SEM analysis, tensile testing, Forming Limit Curve investigation and flange formability testing. The alloys of interest were Dual Phase (DP) untempered, Dual Phase (DP) tempered and Complex Phase (CP) steels. Phase content analysis showed that the distribution of the ferrite and martensite phases was the same for the two DP alloys, but the grain size and condition (tempered/untempered) for the martensite islands was much different in the two alloys. In the tempered DP steel, the smaller grain size for the martensite and the tempering process resulted in increased elongation, more formability and ability to form a flange (flangeability). In CP steels the soft ferrite phase is replaced by harder bainite, yielding a bainitic-martensitic microstructure. Bainite reduced the total elongation of the alloy during tensile testing, reduced the formability (especially under plane strain conditions) of the alloy but improved the flangeability of the alloy. Under flanging conditions, CP steels deformed to higher strains, at tighter radii with minimum springback. Microstructural inspections at the outer radius of the flanged specimens revealed that in CP steels bainite deforms similarly to martensite, therefore the strain partitioning is smaller in CP steels in comparison to DP steels. Plastic deformation in CP steels upon flanging occurs with the formation of strong slip bands in both martensite and bainite. In contrast, the martensite and ferrite grains in DP steels deform quite differently leading to strong strain localisations. Void nucleation and cracking occurred at the martensite islands or within the soft ferrite phase next to the martensite islands. In CP steels no voids or damage was observed within the matrix. A special case study was done with a thicker and stronger alloy, a Martensitic 1400 steel to reveal the flangeability limits for advanced high strength steels. Neither cracks nor damage were observed visually on the flanged specimens. However SEM observations at the outer radius of the flanged samples revealed significant void growth at inclusion sites and cracks nucleating within the matrix adjacent to the inclusions.

1. Introduction

Ultra-High Strength Steels (UHSSs) have emerged in the automotive market due to their superior strength and performance in crash in comparison to low strength steels and other metallic alloys [1–5]. Utilising higher strength alloys allows the design of structural automotive components with decreased thickness, reducing the overall vehicle weight [3–6]. A combination of different phases, such as retained austenite, martensite, bainite and ferrite are developed in these steels giving structural components a broad range of strength and formability. Increasing the percentage of the soft ferrite phase increases the deformability but on the other hand reduces the strength of the alloy with the same chemistry (but different heat treatment). In contrast increasing the percentage of martensite or bainite increases the strength of the alloy but decreases the deformation capabilities of the material [3–5]. Retaining austenite at room temperature can increase both the strength and total elongation of the alloy in Transformation-Induced Plasticity (TRIP) steels. Yet TRIP steels have been found to have weldability issues which restricted their commercial use for car-body chassis [3].

A series of studies exist, where the formability of various engineering alloys is evaluated both experimentally and numerically. The final failure in formed parts is estimated by predicting void nucleation and growth, yield surface curvature and material rate sensitivity in the following studies [7–10]. These studies were limited to isotropic materials [7–10]. However, sheet metals display highly anisotropic behaviour that is introduced when a cast billet is hot or cold rolled into sheet material. Anisotropy is frequently modelled by adding a 'correction' to

* Corresponding author.
E-mail address: P.Efthymiadis@warwick.ac.uk (P. Efthymiadis).

http://dx.doi.org/10.1016/j.msea.2017.06.056
Received 30 March 2017; Received in revised form 12 June 2017; Accepted 13 June 2017
Available online 22 June 2017

existing isotropic models. Liao et. al in his study introduced an anisotropic criterion for the failure prediction of sheet metals under plane stress conditions, based on a modified Gurson yield criterion [8].

Similarly Chien et. al incorporated three additional fitting parameters to the modified Gurson anisotropic yield criterion to account for both the presence of anisotropy and the influence of voids [11]. Chien et al. in a latter study performed a thorough investigation on the failure of Aluminium sheets in a Limiting Dome Height (LDH) test and attributed final failure to the effect of shear localisation; both in cases where the sample showed significant or negligible amount of necking [12]. Chien et al. considered geometric imperfections within the material (such as pores, inclusions, intermetallics etc.) to be responsible for the onset of necking in sheet metals under plane stress conditions. While it was stated that it is material imperfections that result in the shear localisation or the final failure of sheet metals under generalized plane strain conditions. - However it is known that it is not material imperfections but crystal structure, crystallographic orientation and texture that governs the formation of shear bands [13]. - In their FE model, the necking component was excluded from the analysis and only the shear band localisation mode was taken into account. A plane strain formulation was followed where the shear bands form in the through thickness direction. The failure strains on the stretching sides of the bended sheets were estimated by using the failure strains for the LDH samples.

A series of mechanical tests were performed by Bai et al. to obtain the deformability and fracture locus for a wide range of stress triaxialities and sample geometries [14]. The alloys investigated were an Al2024 T351 and a TRIP RA-K40/70 alloy. A modified Mohr-Coulomb (M-C) criterion was employed and showed very good agreement between the experiment and the model for a wide range of shear dominate fractures. Only for round bars under tension the correlation did not match between the experiment and the model. It should be noted though that the specific M-C criterion assumed only material isotropy, but predicted well both the location for crack initiation and the crack directions.

In another study, Hudgins et al. tried to reveal the mechanisms of failure during forming operations in Advanced High Strength Steels (AHSSs) [15]. Hudgins et. al suggested that fractures occurred due to shear dominated mechanisms and led to limited localised necking. Fracture was observed on alternating 45^0 planes, in the through-thickness direction. The strain paths and the fractures occurring during roller hemming operations in AHSSs are difficult to predict using Forming Limit Curves (FLC). The presented model incorporated two components, one to predict instability at die radii, and another to predict tensile failure in the free ligament. An approach was followed in order to predict shear-dominated instabilities at die radii, represented by maximum applied tensile force as a function of die radius. Fig. 1 shows the presence of a transition zone from die instability to tensile instability with increasing the die radius. Material tensile strength is the most important parameter at large radii in contrast to the die geometry for small radii as shown in Fig. 1. A critical radius is introduced (normalized by sheet thickness: R/t_{crit}), above which materials will fail in tension. The critical R/t value is dependent on the slope of instability curve at small radii and the material tensile strength at large radii (Fig. 1). The materials examined showed similar slopes at lower radii, and thus formability for these steels depends primarily on tensile strength.

The formability of a 1050 aluminium alloy was investigated under roller hemming operations in [16]. Muderrisoglu et al. suggested that the roller hemming deformation mechanisms are more complex with respect to simple bending and flanging tests as the stress fields become three dimensional [16]. It was concluded in this study that the flange height (length of flanged sheet in the direction perpendicular to the width of the sheet) has a greater effect with respect to the bend radius on the load necessary to form the part. Pradeau et al. in a latter study developed a model that predicts final failure of aluminium alloy sheets

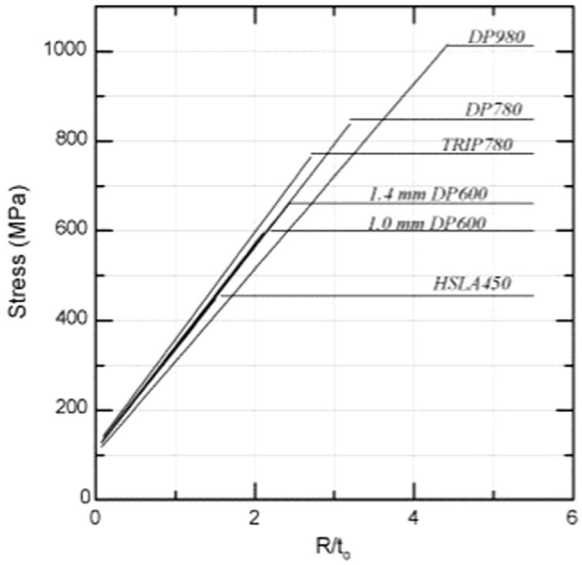

Fig. 1. Theoretical instability curves based on a strain hardening analysis for all studied materials. Similar slopes are observed in the shear fracture region at low radii, forcing the critical R/t ratio to be heavily dependent on tensile strength (after [15]).

during hemming operations based on the Hosford-Coulomb rupture criterion but gave no explanation as to the absence of necking during such operations [17]. The model included an anisotropic yield function, a mixed (isotropic and kinematic) hardening law and a fracture criterion. The comparisons were performed for the load evolution, strain field and prediction of rupture. A very good correlation was obtained over all the tests. The prediction of the developed fracture criterion proved to be successful independent of the amount of pre-strain.

Maout et al. used the Gurson-Tvergaard-Needleman (GTN) model to predict damage nucleation during a hemming process of a 6000 aluminium alloy [18]. Tensile testing of flat and notched samples together with biaxial testing was initially done to optimise the material parameters and allow for the consideration of the different strain paths to damage nucleation and evolution. An FE model of the hemming process was build incorporating the anisotropy of the material. The hemming limit criterion was based on the critical void volume fraction. Criteria of acceptance for the hemming-formed sheets were revealed based on visual observations of the outer radius. The decision to accept or reject components was based on crack lengths and densities.

However, Miller has pursued a thorough analysis on the behaviour of cracks and the safety of engineering components [19,20]. Miller stated that the physics of crack propagation are governed largely on its size and on the mechanical conditions applied [19]. Three different zones can be found in the lifetime of a crack in Fig. 2: the so-called microstructural short crack growth regime (A-B zone), the physically small crack growth regime where Elasto-Plastic Fracture Mechanics concepts can be applied (B-C zone) and the zone where the crack is large enough for Linear Elastic Fracture Mechanics to be applied (C-D zone). In zone A-B crack initiation and growth depends on material microstructure at the grain level. In zone A-B, precipitates or inclusions act as stress concentration points and therefore facilitate crack initiation. The A, B and C barriers are of increasing strength opposing early crack growth. These three barriers can be grain boundaries for example. The microstructure effects have an important role also in the physically short crack region. Yet Fig. 2 shows that the effect of the grains and grain boundaries becomes smaller and smaller as the crack grows. The important zone in Fig. 2 is the microstructurally short crack growth regime where crack growth speeds are very low, governing the overall fatigue life. Fig. 2 also shows why surface finish is important: if surface scratches (or in the case of a formed part surface ripples) are deeper than C, then the structural integrity of the engineering component is

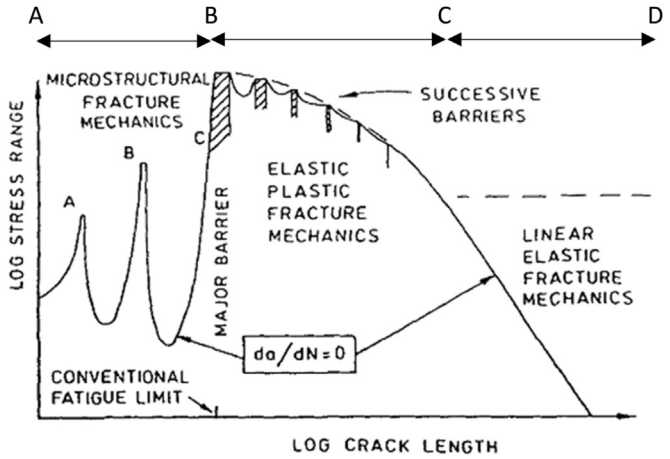

Fig. 2. Regimes in the lifetime of a crack, highlighting the effect of grain boundaries upon crack growth (after [19]).

reduced significantly. The same is true also for the case of scratches and ripples formed during stamping, forming, roll-forming, flanging and roller hemming operations. From this analysis it can be understood that more scientific criteria need to be drawn for the acceptance of cracks in automotive components. Should the crack in hemming formed parts be larger than three grains, then the microstructure has a small effect on the crack growth mechanisms and should the crack be larger than seven grains, Linear Elastic Fracture Mechanics can be applied for crack growth and thus cracks can grow even with the application of small elastic loads. Furthermore, the formation of surface roughness in the part during any given forming operation can act as crack nucleation and growth site, so it should be minimised.

In this study we are particularly interested in the flange forming ability of AHSSs in the higher yield strength range. These grades of steel are difficult to form using traditional press forming technologies, but are easily shaped by roll forming, with flange forming representing the key forming process. Most optimisations of metallic alloys are based on testing the alloys under tension [6]. This is a very simple test but measures mechanical properties under membrane stress conditions rather than the more complex bending stress conditions that are found during flanging. And can therefore be misleading [6,7]. A series of mechanical testing is done to try and understand the mechanical performance of a series of UHSSs. Two Dual Phase (DP) steels with different thicknesses, 1.2 mm and untempered condition, 1.6 mm and tempered condition as well as a Complex Phase (CP) steel with 1.3 mm thickness were evaluated in this study. Both DP and CP steels have found an increasing use in the automotive industry due to their formability and strength. All three alloys had an Ultimate Tensile Strength (UTS) of 1000 MPa. Tensile testing, Forming Limit Curve determination and flanging tests were performed in order to understand the mechanical performance of all three alloys. High resolution SEM analysis was done at the outer radii of the flanged specimens in order to correlate the microstructural performance to the corresponding macroscopic mechanical properties. A study was finally done with a Martensitic 1400 steel to reveal that in some cases visual inspections of formed parts can be sometimes misleading. In most reported papers, sophisticated models were developed which were validated against fairly basic data. The DIC data obtained in this work, combined with the high resolution SEM inspections of the flanged specimens provide a more comprehensive view and experimental data of the nature of the flanging process and the microstructural deformation that takes place.

2. Experimental procedures

Three commercial advanced high strength steel alloys were provided by Tata Steel: DP1000 1.2 mm in untempered condition, DP1000 1.6 mm in tempered condition and CP1000 1.2 mm. Samples were extracted from the sheets and were mechanically polished down to 0.05 μm to reveal their corresponding microstructure. Etching was performed with Nital 0.5% to reveal the phases present in all three alloys. The corresponding micrographs for the alloys are shown in Fig. 3. The red, black and orange arrows indicate the presence of martensite, ferrite and bainite at the respective locations. Fig. 3a shows the DP1000 untempered steel and the presence of two phases, i.e. ferrite and martensite. Fig. 3b shows the presence of ferrite and martensite in DP1000 tempered steel. The grain size and distribution for the hard martensite phase is much different, comparing Fig. 3a and b. CP1000 steel in Fig. 3c consists of bainite and martensite phases.

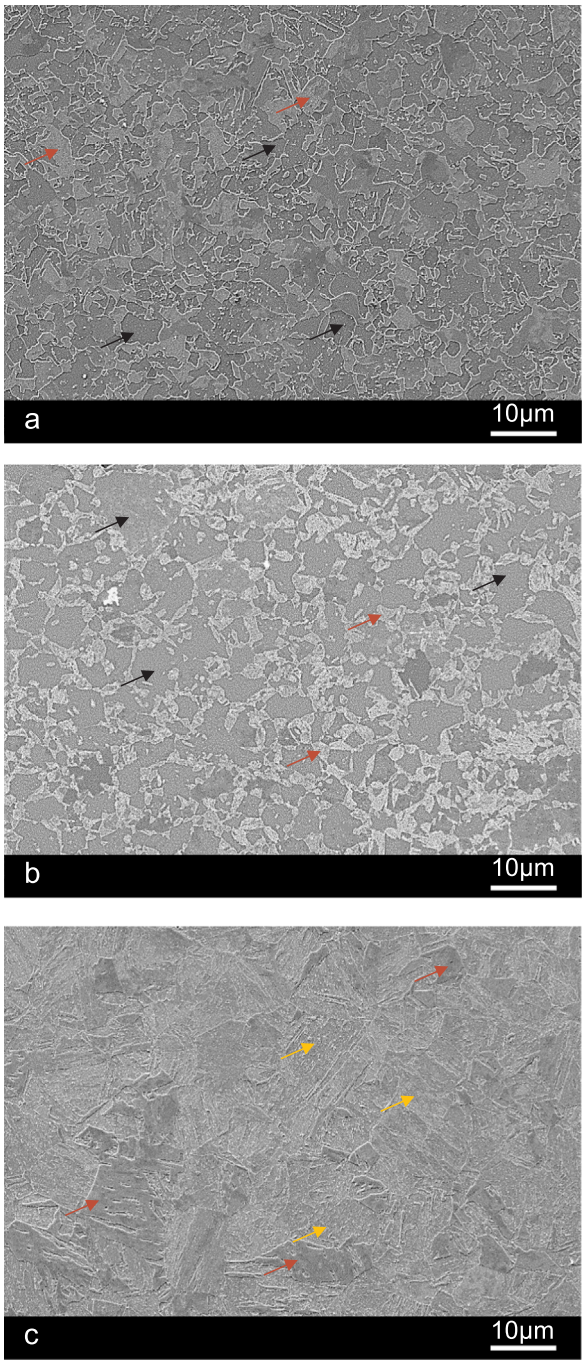

Fig. 3. Microstructural picture of: a) DP1000 steel with 1.2 mm thickness, b) DP1000 Steel with 1.6 mm thickness and c) CP1000 steel. The black, red and orange arrows correspond to the ferritic, martensitic and bainitic regions.

Three types of tests were done in this study: tensile, Forming Limit

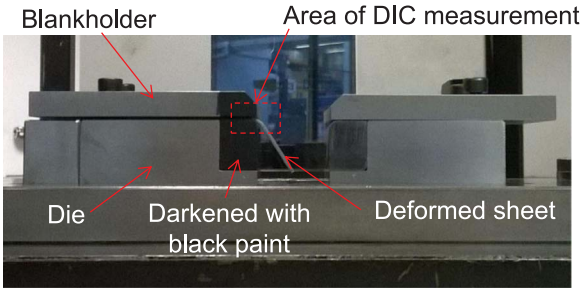

Fig. 4. Experimental set-up for the flanging tests.

Curve (FLC) and flange testing. Tensile testing was carried out with a speed of 2 mm/min, under displacement control. The gauge length was 100 mm and the width of the samples 12 mm. A 70 mm extensometer was employed to accurately measure the strains at the centre of the sample and obtain the stress strain curves for all three alloys. FLC testing was done with a punch speed of 50 mm/min, at displacement control mode. The gauge width for the FLC specimens was: 40 (represents the tensile regime), 60, 80, 100, 120, 140 and 178 mm (full sample; biaxial test). A 5MegaPixel (MP) 3D Digital Image Correlation (DIC) GOM-Aramis system was employed to obtain the strains at the top surface of the specimens throughout the test. From the strain analysis, a post-processing procedure was followed within the GOM-Aramis 6.02 interface to obtain the FLC curve for all sample geometries, for each alloy. A three layer die cover consisting of polytetrafluorethylene, polyurethane and polytetrafluorethylene was employed to minimise the friction between the punch and the specimen during FLC testing.

For flange testing the samples had a geometry of 20 mm width and 100 mm length. Fig. 4 shows the experimental set-up for flange testing. Testing was carried out at a speed of 30 mm/min, under displacement control. The strains through thickness during flange testing were measured by a 12MP 2D DIC GOM-Aramis system. A 25 mm extension tube was attached on the 100 mm lens of the camera during flange testing to increase the lens magnification and allow accurate measurements of the through-thickness strains (1.2–1.6 mm thickness). An additional set of experiments was done for the same flanging set-up. The specimens were initially ground, polished and etched on one side (20 × 100 mm) of the specimens to reveal the microstructure. The specimens were then flanged. The side under tensile regime, where the maximum tensile strains occur corresponded to the polished and etched surface. This procedure was followed in order to observe the microstructural deformation during flange testing and reveal what is happening down to the microstructural level at the top highly-strained free surface upon flanging. Details of this procedure is given later on in Section 3.3.

3. Experimental results

Phase content analysis was performed for all three alloys: DP untempered, DP tempered and CP alloys. The SEM images obtained for each alloy were post-processed with ImageJ software [8–10]. The phase maps were obtained by thresholding the pixel values of the SE micrographs of Fig. 3 with a minimum value of 165 (black pixel) and a maximum value of 225 (white pixel). Fig. 5a and b shows the SEM and the ImageJ post-processed micrograph of DP1000 tempered steel 1.6 mm. The white pixels corresponds to martensite and the black pixels to ferrite in Fig. 5b. The phase content analysis revealed the presence of 67% martensite and 33% ferrite. Similarly DP1000 untempered steel (1.2 mm thickness) consists of 67% martensite and 33% ferrite. Even though the phase content was approximately the same for the two DP alloys, in Sections 3.1 and 3.2 it was found that the respective mechanical properties were very different. This can be attributed to the distribution and size of the martensite islands. In tempered DP1000 steel 1.6 mm the martensite islands are rather smaller and appear to be at the prior austenite grain boundaries. While for the 1.2 mm untempered steel the martensite islands are larger; similar size to the grain size of the ferrite grains. The phase content analysis in CP steel revealed 60% bainite and 40% martensite. The soft ferrite phase in DP steels is replaced by hard and less deformable bainite in CP alloys.

3.1. Tensile testing

Tensile testing was carried out on all three alloys and the corresponding stress-strain curves are shown in Fig. 6a. CP steel has a relatively high yield point (945 MPa), low UTS point (1011 MPa) and limited elongation capabilities (total strain: 0.082) in comparison to DP steels; as shown in Table 1. The DP1000 untempered and DP1000 tempered steel had a low yield point, high UTS and total elongation which were: 718 MPa and 736 MPa, 1066 MPa and 1059 MPa, and finally 0.117 and 0.123 respectively. The curve for the CP steels have a plateau in the plastic region with minimum work hardening ($n = 0.044$) in comparison to DP steels which had approximately 0.13 n-value. This is due to the presence of the hard bainite phase which increases the yield point and stresses in the elastic region; in comparison to the soft and deformable ferrite phase which decreases the yield point however allows for higher work hardening rate. The DP1000 1.6 mm has slightly lower work hardening rate ($n = 0.124$) in comparison to untempered DP1000 which had a value of ($n = 0.144$). Tempered DP1000 has also higher UTS point and slightly larger total elongation (30 MPa and 0.04 stress and strain difference). FLC testing revealed that CP steels have lower deformation capabilities in comparison to DP steels, especially under plane strain condition (Fig. 6b). The major strain under plane-strain conditions is on average 0.08 for the CP steels. While for the DP untempered and tempered alloys was 0.12 and 0.13 respectively. Under uniaxial loading conditions, the major strain was 0.16, 0.23 and 0.26 for the CP, DP untempered and DP tempered. Only under biaxial testing conditions both DP and CP alloys had similar deformation capabilities.

3.2. Flange testing

3.2.1. Load-displacement results

Flanging was performed with the set-up outlined in Fig. 4. The corresponding load-displacement curves for all three alloys are shown in Fig. 7. The load decreases linearly with extension after an extension of 8.5 mm, following an inclination of −74.2° for DP1000 untempered and CP1000 and −77.4° for DP1000 tempered alloy. DP1000 tempered steel had higher load capabilities with respect to DP1000 untempered and CP1000. This is due to the increased thickness; i.e. 1.6 mm. The lowest load capacity corresponds to DP1000 untempered, which was 1100 N. In CP alloys, work hardening occurs upon further extension between the initial load peak at 2.5 mm and up to 8.5 mm extension. This can be related to the presence of bainite in the matrix which requires higher loads upon further plastic deformation with respect to the soft ferrite phase in DP steels. The load-extension curve for CP1000 lies in between the two DP steels, for flanging extension larger than 8.5 mm. This suggests that CP steels require higher loading conditions during flanging operations in comparison to DP alloys. After flanging, CP steels can withstand higher loads in a structural component subject to flanging and bending moments.

The springback during flanging was also measured for the three alloys and is shown in Table 2. The amount of springback was calculated as follows. The angle of the flanged and deformed specimen was measured from the image captured via GOM-Aramis software for two sample conditions: for the fully displaced and fully loaded configuration and for the full deformed but unloaded configuration. This way the elastic recovery of the sample was measured. The results are shown in Table 2. The lowest springback was measured for CP steels with an average value of 8.1°. DP tempered and untempered steels had a springback value of 10.0° and 10.8°.

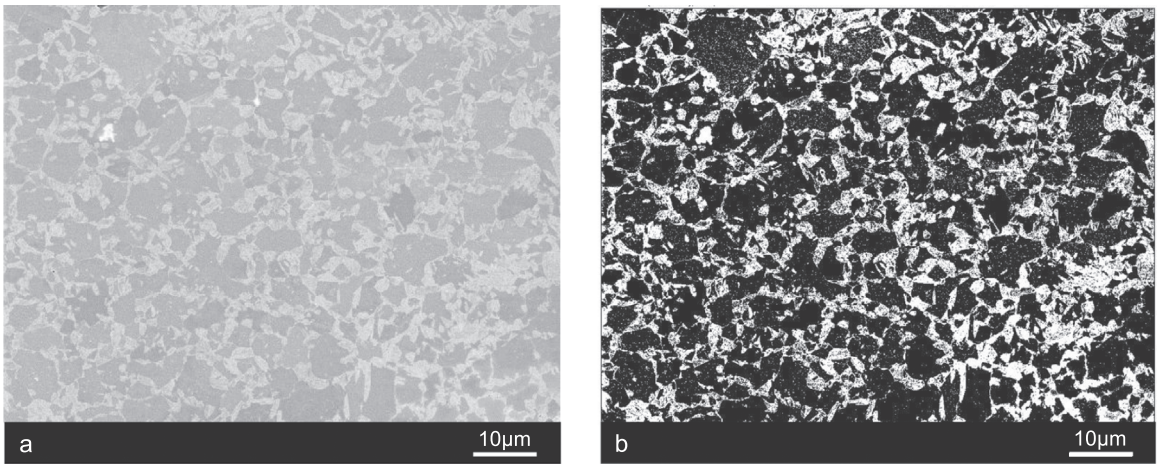

Fig. 5. a) Microstructural picture taken with a FEG-SEM Zeiss Sigma and b) the corresponding processed image with ImageJ software of the SEM image of Fig. 5a.

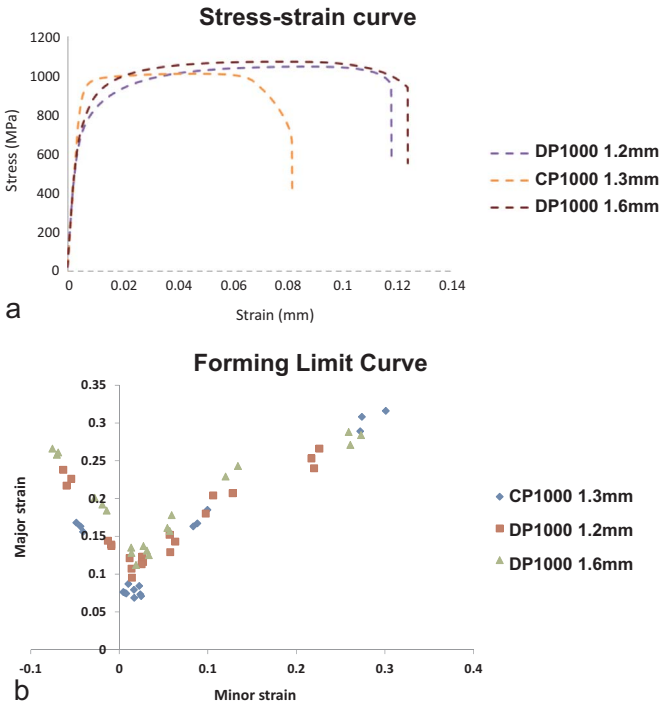

Fig. 6. a) Tensile curves for all materials, b) FLC curves obtained.

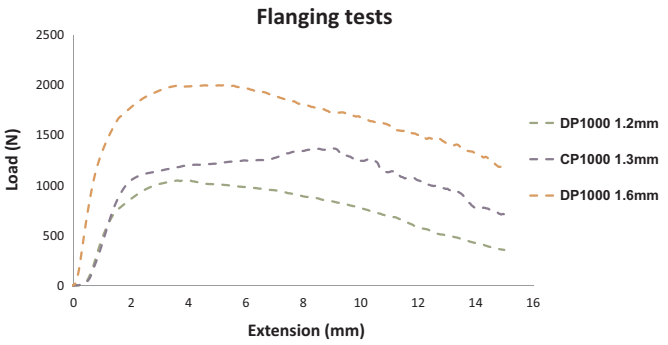

Fig. 7. Load-displacement curves for three alloys DP1000 untempered, DP1000 tempered and CP1000 alloys.

Table 1
Data obtained from tensile testing and flange testing for the three alloys: DP1000 1.2 mm, DP1000 1.6 mm and CP1000 1.3 mm.

Material	Yield Point / 0.2% offset (MPa)	UTS point (MPa)	Total elongation
DP1000 (1.2 mm)	718	1066	0.117
DP1000 (1.6 mm)	736	1059	0.123
CP1000 (1.3 mm)	945	1011	0.082

Table 2
Springback effect for the three alloys.

Sample	Before springback^0	After springback^0	Springback^0	Average^0	Yield Ratio
CP1000 (1.3 mm)	65	57.2	7.8		
CP1000 (1.3 mm)	65.6	57.2	8.4	**8.1**	~0.95
DP1000 (1.2 mm)	66.9	56	10.9		
DP1000 (1.2 mm)	66.7	56	10.7	**10.8**	~0.7
DP1000 (1.6 mm)	66	56	10		
DP1000 (1.6 mm)	66	56	10	**10**	~0.7

3.2.2. Strain analysis

A 12 Megapixel (MP) 2 Dimensional (2D) Digital Image Correlation (DIC) system was employed to measure the through-thickness strains during flange operation. The major strains were measured at the outer radius of the specimen during flanging to obtain the highest strains for all three alloys: DP untempered, DP tempered and CP steel. Fig. 8a shows an image captured with the DIC camera during the flanging operation. The image was DIC post-processed and the strains were measured through the thickness. Fig. 8a shows the location where the highest strains were observed and the major strain development during flange testing. The highest strains correspond to the top surface of the flanged specimens and were 0.201 for CP steels, 0.198 for the thicker DP tempered steel and 0.158 for the thinner DP untempered alloy. The major strain development at the top surface (arrowed location of Fig. 8a) throughout the test for all three alloys is shown in Fig. 8b. At the first stages of plastic deformation during flanging, CP steels appear to have the lowest strains, however after a certain point (15 s), significant strain development occurs with respect to the other two alloys.

Table 3 shows a comparison between the Ultimate Tensile Strength (UTS) and total strains obtained from tensile testing to the major strains obtained at the outer radius upon flange testing. During flange testing, the maximum strain was higher than the UTS and final failure strain from the tensile test for all three alloys. Visual inspections in all alloys after flanging revealed no indication of cracks at the top surface. DIC

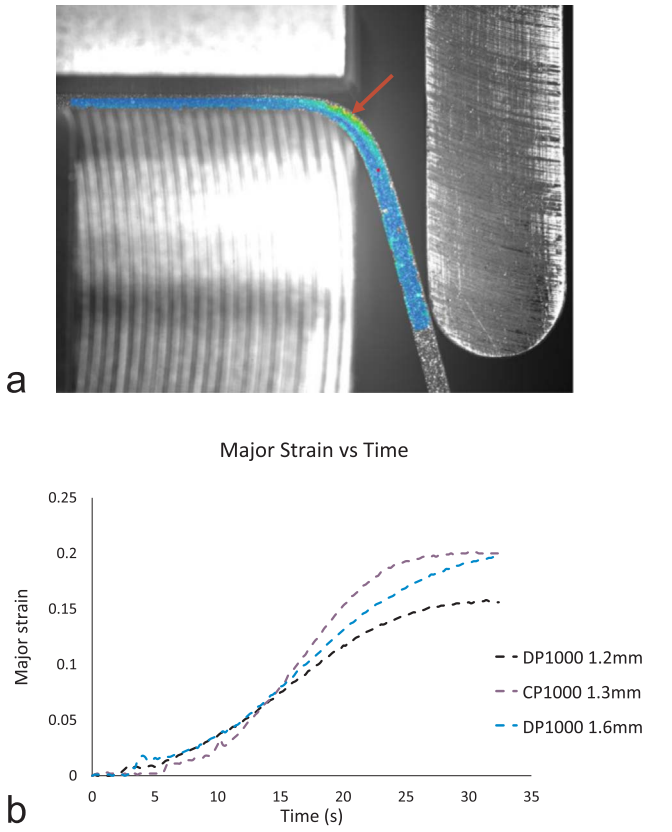

Fig. 8. a) Major strains measured at the top surface of the specimens. Red arrow shows the location where the highest strains occur during flanging. The specimen thickness is 1.2 mm. b) Plot of the major strains during flanging for: DP1000 untempered (1.2 mm), DP1000 tempered (1.6 mm) and CP1000 steel (1.3 mm).

Table 3
Data obtained from tensile testing and flange testing for the three alloys: DP1000 1.2 mm, DP1000 1.6 mm and CP1000 1.3 mm.

Material	Tensile strain (at UTS)	Total strain	Peak bending strain
DP1000 (1.2 mm)	0.09	0.12	0.158
DP1000 (1.6 mm)	0.07	0.125	0.198
CP1000 (1.3 mm)	0.045	0.08	0.201

measurements showed there is significant strain variation through the thickness of the sheets, however there are no strong strain variations at the arrowed location of Fig. 8a which can indicate the formation of cracks at the top surface (arrowed location). The highest strains were measured for the CP steel (strain of 0.201) which had the minimum elongation capabilities during tensile testing (strain of 0.08).

3.3. Microstructure-properties relationship during flanging operations

The specimens were ground, polished and etched at one side of the specimens (20 × 100 mm). The undeformed and deformed (flanged) specimens are shown in Fig. 9a and b. Four alloys have been flanged; the CP1000, DP1000 untempered, DP1000 tempered steel and Martensitic1400 steel. The last alloy was added in this part of the study, in order to signify the importance of doing SEM microstructural observations in formed parts. Inspections were performed with a FEG-SEM at the top surface, at the arrowed location of Fig. 8a, on the highly deformed region of the flanged samples. The next four sections present the results for the four alloys. Prior to SEM inspection the samples were visually and optically inspected without any evidence of damage.

3.3.1. Flanging of DP1000 untempered steel

High resolution SEM inspections at the top surface (arrowed location of Fig. 8a) of the DP1000 untempered steel revealed the highly non-homogeneous strain fields at the microstructural level upon flanging operations. It has been reported in other studies that during tensile testing, the strain fields are also highly non-homogeneous for multiphase steels due to the deformation mismatch between the different phases [12–15]. This mismatch results in higher strains concentrating in the softer matrix. Upon flanging, as it occurs during tensile testing, most of the plastic deformation is taken by the soft ferrite matrix. Slip bands were observed to have formed within the individual ferrite grains as shown with the red arrows in Fig. 10a, b, c and d. The slip bands cross through several grains as shown in Fig. 10c and d, forming shear bands close to 45° with respect to the loading direction (horizontal axis). The direction and width of the slip bands can be approximately the same within the individual grains as shown with the black arrow in Fig. 10b, but in most cases such as in the red arrowed locations in Fig. 10 is not constant for both the width and the orientation/direction. This is due to the irregular morphology of the neighbouring martensite islands and local misorientations within the ferrite grains. In most cases the slip bands cannot travel through the hard martensite islands, which leads to two mechanisms for damage nucleation: fracture of the martensite islands (at the yellow-arrowed locations in Fig. 10a and b) and more frequently void nucleation in the soft ferrite phase next to the ferrite-martensite interfaces (yellow-arrowed locations in Fig. 10c-e). Low magnification SEM imaging of Fig. 10f also revealed that the strain fields can highly localise at a soft ferrite path where several neighbouring ferrite grains lie perpendicular to the loading direction. Such ferritic regions can be related to the solidification processes and the formation of dendrites in cast steel slab prior to the steel sheet rolling process. Deformation in DP1000 untempered steel takes place in the soft phases and is obstructed by the hard phases, thus limiting the formability of the alloy. This is in accordance to numerous other studies [12–15].

3.3.2. Flanging of DP1000 tempered steel

The top surface of the flanged DP1000 tempered alloy revealed the presence of slip bands within the ferrite matrix. Most deformation is accumulated within the soft ferrite matrix. However it can be seen in Fig. 11a that the slip bands cross through the hard and tempered martensite without creating any voids within the matrix. The voids in the DP tempered alloy were smaller with respect to the DP1000 untempered alloy and their occurrence was much less observed. In a scanned area of 500 μm × 500 μm, the DP tempered steel had just 7 voids of size smaller than 1 μm, with two voids reaching a size of 1.5 μm, while in the case of untempered DP, the voids were 25, with the average size being approximately 1.5 μm with five voids having a size of 3 μm. Typical voids that nucleated within the matrix of DP tempered alloy are yellow arrowed in Fig. 11b-f. Voids formed more frequently within the soft ferrite phase as shown in Fig. 11b, but also within the tempered martensite as indicated in Fig. 11c, at the ferrite-martensite interface as found in Fig. 11d or close to the ferrite-martensite interface within the ferrite matrix as seen in Fig. 11e and f. The thickness of the tempered alloy was also larger which suggests that more voids should be expected during bending and flanging operations. However the opposite trend has been observed suggesting that DP1000 tempered steel has higher flangeability. Furthermore, as shown in Fig. 11a, the slip bands are able to go through the hard martensite phase without any observed damage in most cases. While the deformation mismatch between the soft ferrite phase and the deformation resistant martensite in the case of untempered DP1000, leads to damage nucleation either by martensite fracture (breaking the island in two pieces) or void nucleation within the ferrite next to the ferrite-martensite interfaces. The voids in DP1000 tempered steel were more globular and formed in a small part of the martensite island - such as in Fig. 11c - without cracking or breaking the martensite island in two pieces. As the size of

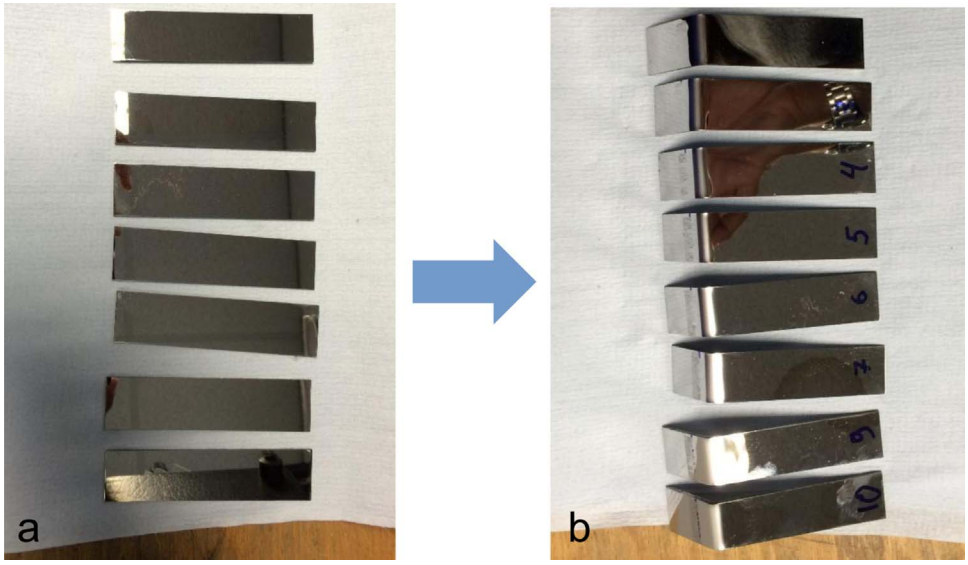

Fig. 9. a) Undeformed samples and b) test pieces after flanging. The width of the samples is 20 mm.

the martensite islands was smaller in DP1000 tempered steel, the voids that formed within or next to the martensite islands were also smaller in comparison to DP1000 untempered steel. This improves further the deformability of the alloy.

3.3.3. Flanging of CP1000 steel

The top surface of the CP1000 steel revealed the highly anisotropic and non-homogeneous strain fields at the microstructural level upon flanging operations. This is indicated in both micrographs of Fig. 12a and b. The strain fields appear highly localised due to the formation of strong slip bands in Fig. 12a. The slip bands appear to have a well-defined step which appeared to be macroscopically perpendicular to the loading direction and through the thickness; in the direction of out-of-plane cutting (as shown by the black arrow head in Fig. 12a). The slip bands are wider and also appear to have a well-defined step in the direction of the black arrow of Fig. 12a. These steps at the microstructural level form due to the dislocations that exit the material as the specimen is deformed upon flanging. The direction of out of plane cutting is the through-thickness direction and these steps form due to the through thickness stresses acting upon flange operations. The presence of high local crystallographic misorientations for the individual platelets in the bainitic regions, affects strongly the path and direction of the formed slip bands. The red-broken line in Fig. 12b shows the path of the slip bands. The slip bands are the results of dislocations that have exited the material. There needs to be a large density of dislocations traveling along the same slip system and exiting the material in the out-of-plane direction to form these well-defined surface steps (along the strong slip bands). The most important parameter that defines which slip system is activated is the local crystallographic orientation. So depending on the local crystal orientation, different slip systems are activated within the corresponding grains/crystals which strongly influences the direction of the formed slip bands. The misorientations for the path of the slip bands, are also related to the misorientations in the underlying bainitic matrix and to the crystallographic mismatch between the neighbouring grains. Extensive observations were carried out on the top sheet, but no damage was observed within the matrix. This can be related to the fact that CP steels, containing bainite and martensite, behave almost like a single phase alloy, with slip bands forming within the two phases at orientations depending on the local crystal orientation. Fig. 12c shows a slip band going through a martensite island at the arrowed location without causing any local failure. In the DP steels the strain mismatch between ferrite and martensite is higher in comparison to bainite and martensite, which leads to damage nucleation in the neighbourhood of the martensite islands. Void growth was found to occur at inclusion sites, but that was also observed in DP steels as well. However in all three cases void growth was contained at the inclusion site without any propagation in the surrounding steel matrix. The two micrographs of Fig. 12e and f, show the occurrence of grain boundary sliding. A martensite grain is present at the yellow-arrowed triple point and has slid along the red-arrowed interface. No failure has occurred at the corresponding site. Grain boundary sliding has mainly been observed at high homologous temperatures in metallic alloys, but can also occur at room temperature; such observations were also made for Aluminium alloy Al2024 upon cyclic testing at room temperature [21].

No local failures were observed for CP1000 steel in contrast to the two DP alloys, which is related to the deformation behaviour of the two phases of the alloy; i.e. bainite and martensite. Both phases deform in similar manner, by the formation of strong slip bands. While in the two DP alloys, slip bands formed in the soft ferrite phase, which in some cases could not go through the hard martensite phase and lead to void nucleation at the neighbourhood of the martensite islands.

3.3.4. Flanging of martensitic1400 steel

A special case study was investigated with flanging martensitic steel with 1400 MPa UTS and 2 mm thickness. This was done in order to emphasize the importance of performing SEM observations at the top surface of the flanged specimen. In most cases engineers access the quality of the formed part visually which can be in some cases misleading. A less formable Martensitic steel was flanged and then visual inspections were carried out similar to the previous Section 3.3. No evidence of damage was observed.

High resolution SEM inspections at the top surface of the Martensitic 1400 steel revealed the highly non-homogeneous strain fields at the microstructural level upon flanging operations. The strains appear highly localised perpendicular to the loading direction. In most cases, these highly deformed regions such as in Fig. 13a-c, did not have any damage but were actually the result of shear deformation in the out of plane cutting direction. The influence of the inclusions was found to be significant for this alloy, the red arrows in Fig. 13a indicate the increase in the width of these bands of out of plane sheared matrix. The red arrows in Fig. 13b indicate the presence of microcracks that have nucleated along two heavily deformed shear bands. Both bands formed due to the presence of inclusions. Fig. 13c shows that the width of the out-of-plane shear band is significantly larger with respect to the shear and formed in the surrounding matrix. Excessive void growth has occurred at the inclusion site which lead to increased elongation in the surrounding martensitic matrix and propagation of the high straining to the surrounding matrix at an angle perpendicular to the loading

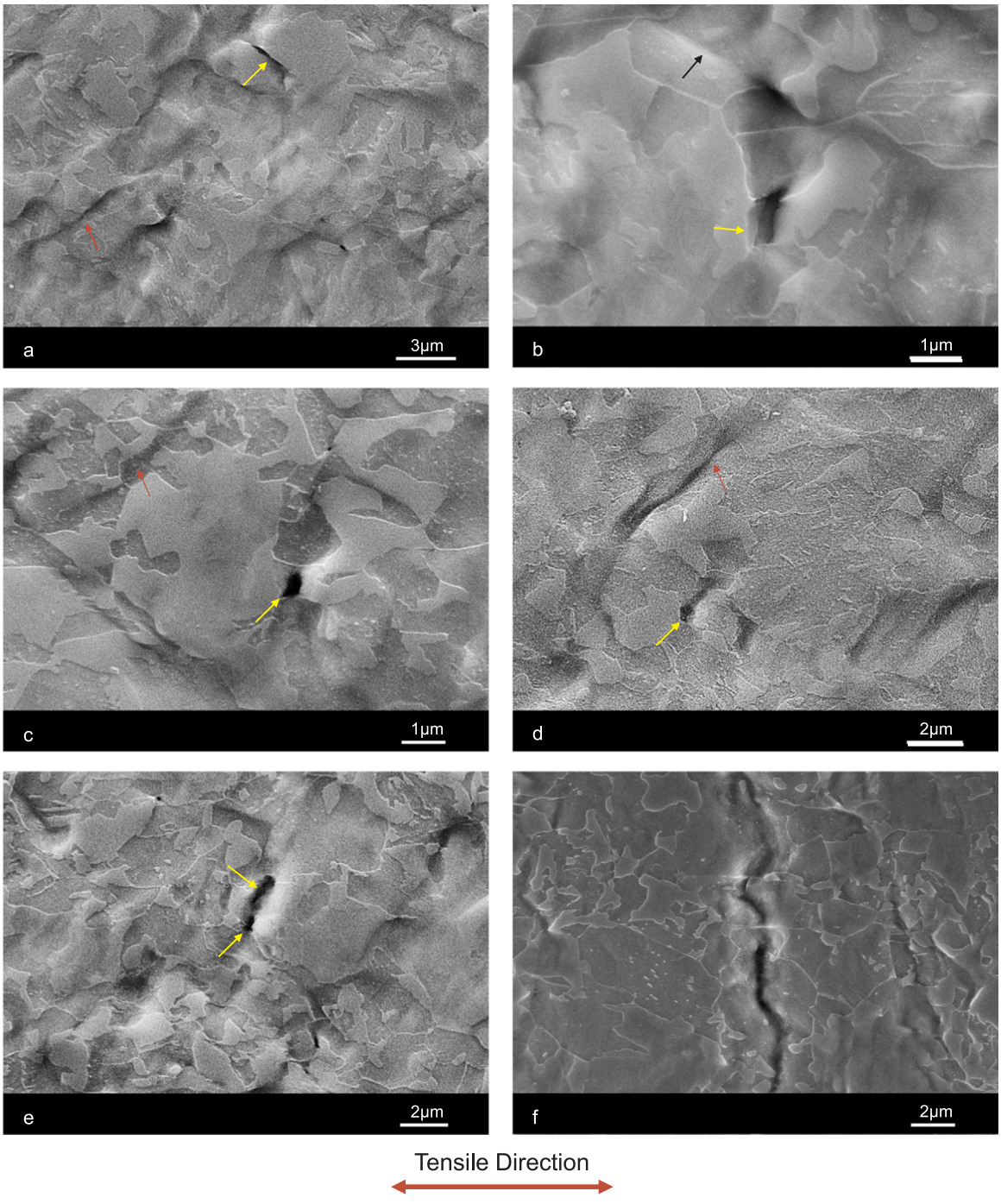

Fig. 10. SE images showing damage nucleation and evolution after flanging for DP1000 1.2 mm thick. a-b) Fracture of the martensite islands occurs at the yellow arrowed locations, c-e) void formation at the yellow-arrowed locations within the soft ferrite grains next to the interface with the hard martensite islands and f) a soft ferritic path localising deformation and damage. (For interpretation of the references to color in this figure legend, the reader is referred to the web version of this article.)

direction; maximum normal stresses. Cracks were found to form along these out of plane shear bands, as shown in Fig. 13e and f. Further investigation and surface inspections revealed that these cracks can both nucleate from the inclusion site such as in Fig. 14a, but also far from the inclusion site and along the same heavily deformed shear band. The mechanisms of the formation of these cracks is a cooperation of two load mechanisms, namely out of plane cutting and normal to the horizontal direction load direction, leading to the microcracks shown in Fig. 14c. Cracks sheared in the out-of-plane direction and opened perpendicular to the loading direction.

These bands of shear localisation in the out-of-plane direction were found to propagate in distances more than 200 μm away from the inclusion site as shown by the red arrow of Fig. 15a. The size of the inclusions was found to be of great importance as well. Relatively small inclusions (smaller than 15 μm) were not large enough to highly localise the stresses and strains. Fig. 15b shows an inclusion of less than 10 μm which is present adjacent to the heavily deformed shear band indicated with a black arrow. The shear band is the same band as in Fig. 15a. All strain localisation occurred along the heavily deformed shear band shown with black arrow in Fig. 15b and no significant strain localisation occurs adjacent to the small inclusion shown with red arrow.

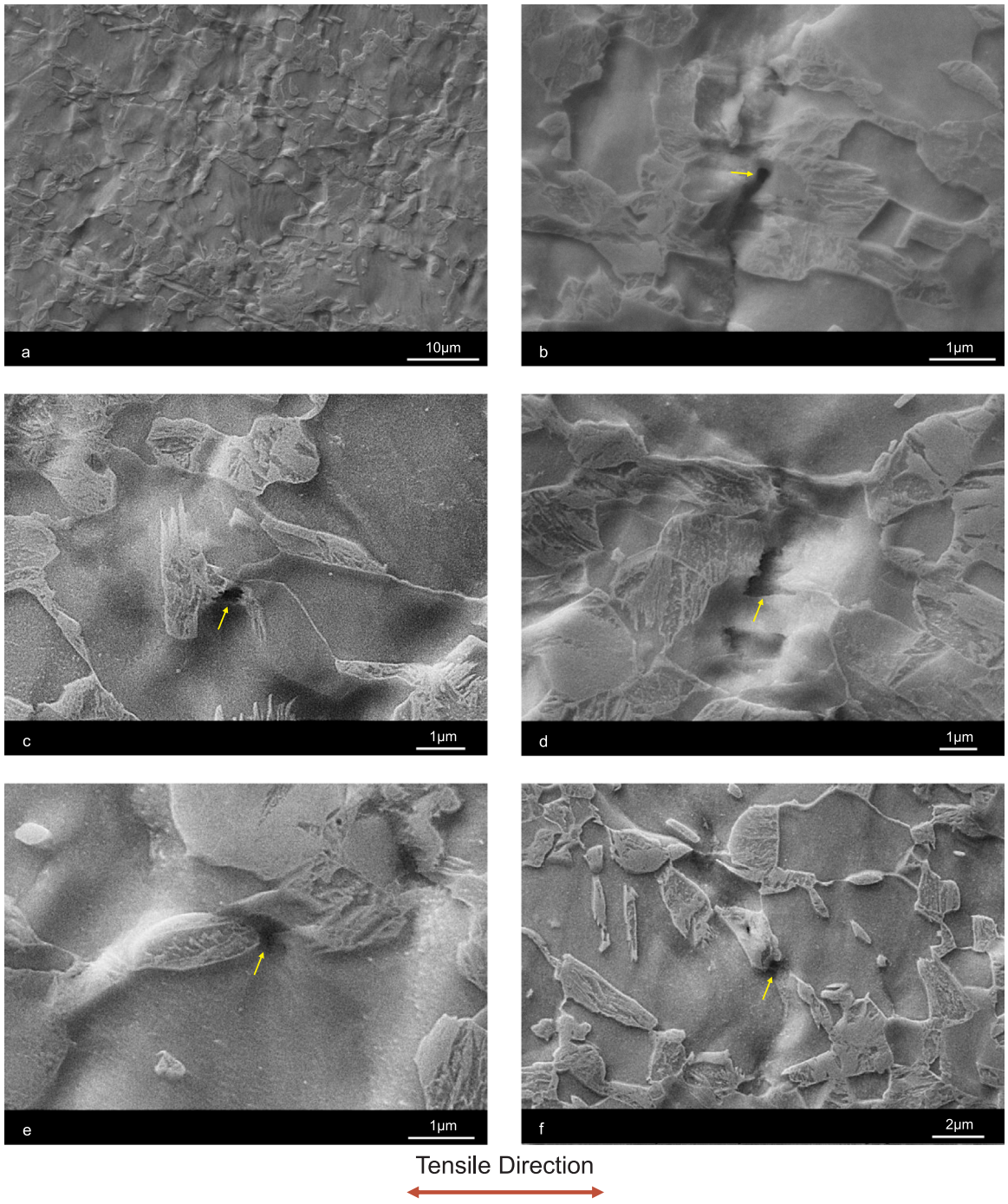

Fig. 11. SEM micrographs after flanging the DP1000 tempered (1.6 mm) steel a) Strain localisations occur within the soft ferrite matrix, b) Strain localisation in the soft ferrite phase leads to void nucleation within the ferrite, c-d) Void nucleation within tempered martensite, e-f) void nucleation within the ferrite phase next to the martensite island. (For interpretation of the references to color in this figure, the reader is referred to the web version of this article.)

4. Discussion

Phase content analysis was done with ImageJ software on the DP and CP steels to reveal the percentage of the corresponding phases, i.e. ferrite, martensite and bainite [22–24]. The two DP alloys have similar phase content, however the size, condition (tempered or untempered) and distribution of the hard martensite islands is much different for the two alloys and therefore the two steel series yield much different mechanical performance.

A detailed analysis was carried out to reveal the differences in type of formability between the three alloys, including performance under flanging operations. The different mechanical performance for the three alloys (DP untempered, tempered and CP) can be attributed to the distribution of the phases, to the grain size and to the condition of the hard phases: tempered or untempered. For the two DP steels, the phase content was approximately the same, however the grain size for the hard martensite islands is much smaller in DP tempered steel. Furthermore, the martensite islands are tougher in the tempered condition, reducing the potency for crack nucleation within the hard martensite islands. In CP steel the soft ferrite phase is replaced by stronger and less deformable bainite which suggests that the total elongation is reduced. The observations made in Fig. 3 are in agreement with the stress-strain curves of Fig. 5, where the CP alloy has the lowest elongation but highest yield point. So replacing ferrite with bainite,

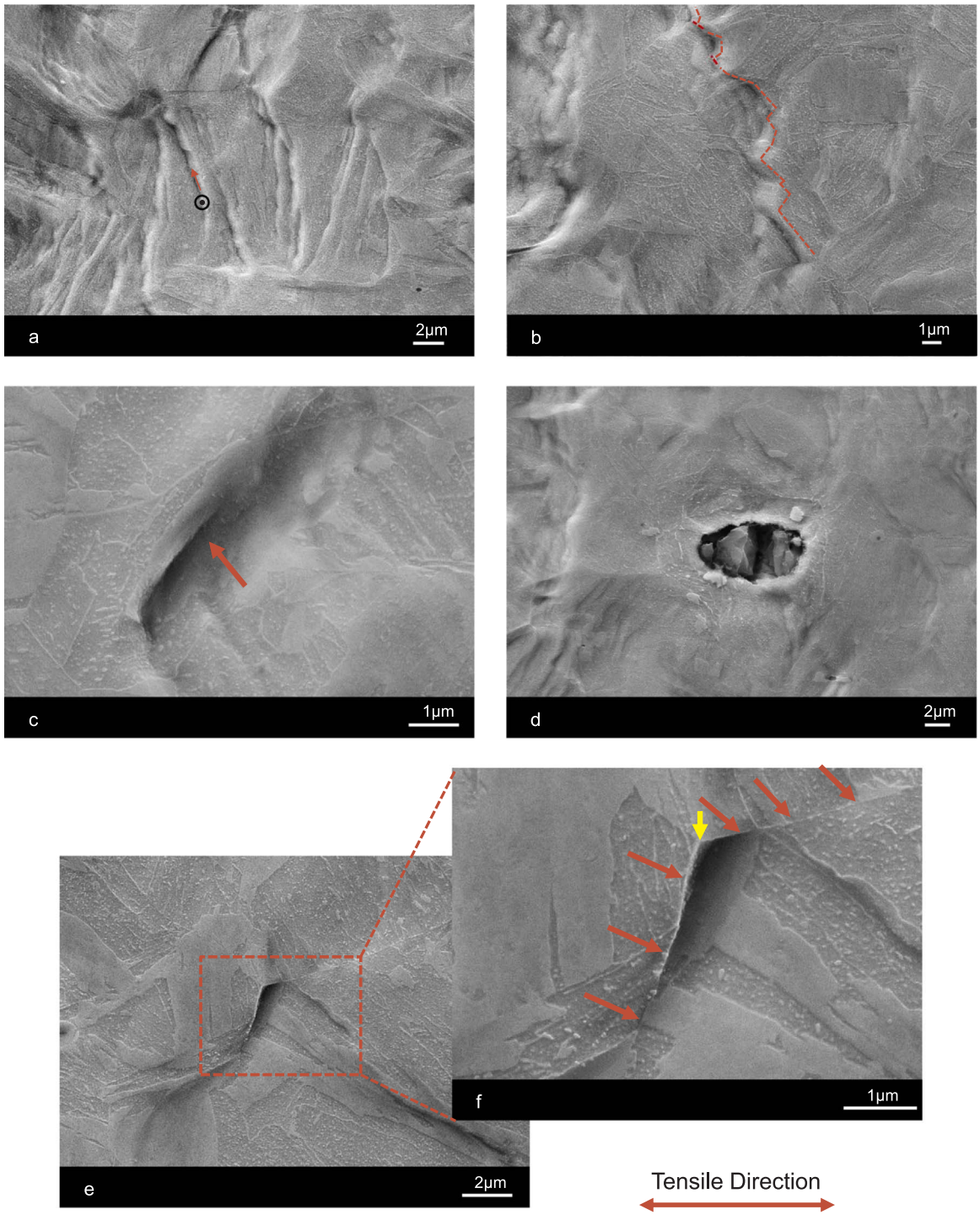

Fig. 12. Strain localisation after flanging for CP1000 steel, a-b) surface inspections showing the formation of slip bands within the bainitic matrix (such as the one shown by red arrow and red broken line, c) slip band formed at the red arrowed location within the hard martensite phase, d) void growth at inclusion site and e-f) plastic slip at the interface shown with red arrows. (For interpretation of the references to color in this figure legend, the reader is referred to the web version of this article.)

increases the yield point but reduces significantly the total elongation by 33%, comparing the DP 1.2 mm thick with the CP 1.3 mm thick alloys. The DP tempered alloy had the highest total elongation.

Flanging tests were done with a 3 mm internal radius to reveal the load-displacement curves. All alloys had the same slope for the curves after 9 mm of displacement. Unlike tensile, CP steels after an initial 4 mm displacement show significant hardening with respect to the DP alloys, raising the load capacity, necessary for further flanging operation. The load displacement curves for the CP alloy lies in between the thin DP and the thick and tempered DP alloys. The higher load for the CP steel can be related to the presence of bainite instead of the soft ferrite phase in DP steels, increasing the local bending stiffness of the sheet under flanging operations.

The major strains were measured at the top radius of the sheets to measure the maximum strains reached for all three alloys. The highest strains were measured for the CP steel, 22% peak bending strain in comparison to 19% and 15% for DP tempered and untempered. This suggests that tighter radius is formed when using CP steels in comparison to DP steels. The amount of springback was also significantly lower for CP1000 steel, even though the yield point was much higher

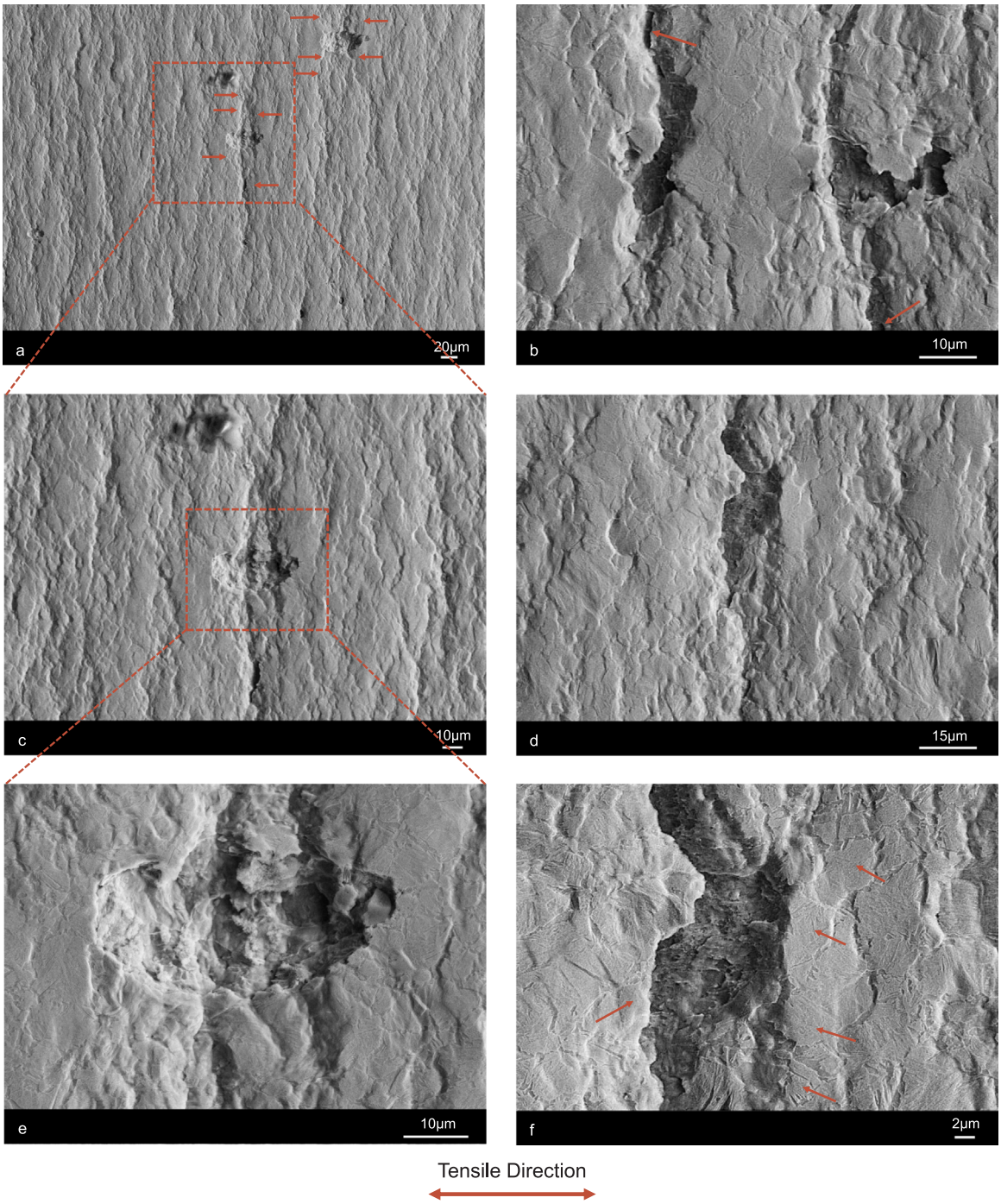

Fig. 13. a, c and e) Deformation and damage localisation at an inclusion site, b, d and f) cracks nucleated along the heavily-deformed regions within the matrix. (For interpretation of the references to color in this figure, the reader is referred to the web version of this article.)

(~200 MPa) in CP steels with respect to the two DP alloys. This was related to the microstructural differences and the different deformation mechanisms between CP and DP steels. Flanging was done in the same alloys, for samples polished and etched prior to flanging operation to reveal the deformation mechanisms at the microstructural level.

Fig. 10 revealed the presence of local failure in DP untempered steel by two mechanisms: a) void nucleation in the soft ferrite phase next to the martensite islands due to the deformation mismatch between the two phases and b) fracture of the hard martensite islands [26–29]. Most of the deformation appeared to be within the soft ferrite phase, with the formation of slip bands, with macroscopic shear bands running through several grains by the adjoin of slip bands within the individual grains [21,26,27]. Fig. 10f reveals a deteriorating material condition where several soft ferrite grains are aligned perpendicular to the loading direction and a soft ferrite path localises the strains at a very small region. These features are damage prone and can lead to the formation of large macroscopic crack in the sample upon further flanging operation.

In comparison to the DP untempered alloy, the tempered DP steel had much smaller void occurrences, in most cases in the soft ferrite phase next to the martensite islands, but also within the martensite islands. Yet the voids were much smaller in comparison to the DP untempered alloy. The average void size was 65% smaller and the number of occurrences 3–4 times less in the DP tempered alloy.

For the CP steel, strong slip bands in the form of well-defined steps which correspond to individual slip systems activated within the individual bainitic regions were found in Fig. 12a and b. No voids or

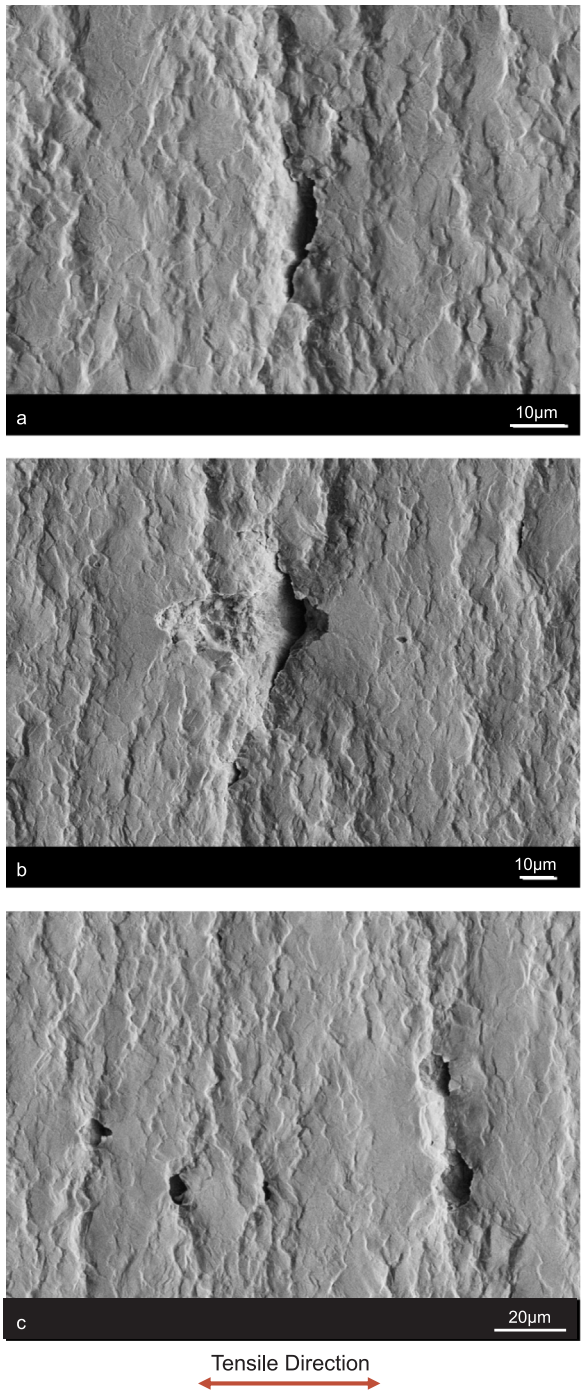

Fig. 14. Deformation and damage localisation along the heavily-deformed regions.

evidence of damage was observed within the matrix. Only some void growth at inclusion sites, which can be expected to occur also in the DP alloys. So CP steels require higher loads upon flanging operations and thus it provides a better strength and bending stiffness for automotive chassis components where flanging operations are used such as in Roll Forming. Furthermore, the component is better formed around the radius as tighter radii can be achieved with less springback. The benefits of replacing ferrite by bainite were also found in the microstructural images of Figs. 10–12, where no damage was observed for CP steel. This behaviour can be attributed to the considerably high deformation mismatch between ferrite and martensite in DP steels. The two phases deform very differently leading to large stress and strain localisations. In comparison, the CP steels behave like a single phase alloy, where the hard phase composes of bainite and martensite. Both phases deform similarly and the strain gradients at the interfaces between the different phases are much smaller in comparison to DP steels [25].

Flanging in the martensitic steel revealed the deleterious effect of inclusions which highly localised the plastic deformation around their neighbourhood. This lead to significant void growth, shear deformation mechanisms in the adjacent matrix and potentially crack formation within the matrix. The highly shear-strained regions were aligned perpendicular to the loading direction and initiate at the matrix adjacent to the inclusions. Strains are initially localised within and adjacent to the inclusion. Considerable plastic deformation takes place, which results to increased void growth, which in turn initiates shear bands next to the inclusions. Upon further plastic deformation cracks can form along these heavily-deformed shear bands. Within these regions microcracks as large as 50 μm were found as far as 300 μm away from the inclusions. Even though these cracks were not visually seen, it should be expected that in highly stressed components such microcracks may lead to final failure [19,20]. These cracks can also lead to oxidation and corrosion problems within the interior of the sheet [30]. Furthermore, Fig. 13f shows that these cracks are no longer microstructural cracks as they extend over several grains and behave like macroscopic cracks which can propagate even when the specimens/components are elastically loaded [19–21]. No evidence of plastic deformation can be seen by the red arrows shown in Fig. 13f. Fig. 15 shows the inclusion size effect. Larger inclusions have a detrimental and crucial impact on the formation of cracks in comparison to smaller inclusions which avoid to highly localise the strains.

5. Conclusions

Tensile, Forming Limit and Flanging tests were performed on Dual Phase, Complex Phase and Martensitic steels to correlate the different microstructures and phases with the resulting mechanical performance. DP steels showed increased elongation but lower yield point in comparison to CP steels upon tensile testing. Similarly the formability tests revealed that DP steels are more formable, especially for the plane strain condition. Yet upon flanging operations, CP steels, showed less springback, formed better around the radius of the tool and also showed no signs of local failure at the microstructural level. It is concluded that using a simple tensile test can be a misleading predictor for the material's performance. Multiscale experimental procedures, both in-situ and ex-situ as in this study can reveal a better understanding about the macroscopic mechanical performance. In this case the deformation mismatch between ferrite and martensite leads to micro voids and small cracks formed within individual grains. In contrast the CP steel deformed like a single phase alloy, as the strain partitioning between the bainite and martensite is much smaller in comparison to ferrite and martensite.

Flanging of martensitic steels revealed that the presence of inclusions in such alloys is detrimental for damage nucleation as excessive void growth at the inclusion sites led to microcrack formation towards the neighbouring matrix. In contrast damage was constrained at the inclusion sites by the neighbouring deformable matrix in the case of DP and CP steels.

Acknowledgements

The authors would like to thank the Engineering and Physical Sciences Research Council for funding this work (Grant EP/M014096/1). The material was supplied by Tata Steel Europe. The authors would like to acknowledge the constant support, assistance and advice provided by Jaguar Land Rover, Hadley Industries plc and data M Sheet Metal Solutions GmbH.

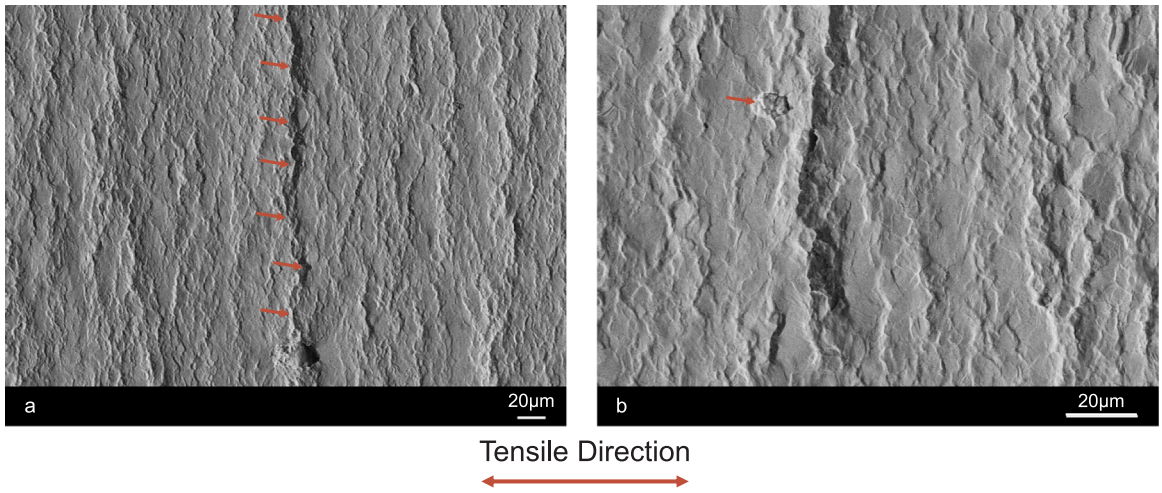

Fig. 15. Inclusion size effect. a) A large inclusion localising the strains perpendicular to the tensile loading direction, b) a smaller inclusion with no strain localisations after flange testing. (For interpretation of the references to color in this figure, the reader is referred to the web version of this article.)

References

[1] J.Y. Koo, G. Thomas, Design of duplex low carbon steels for improved strength: weight applications, in: A.T. Davenport (Ed.), Formable HSLA and dual-phase steels, AIME, New York, 1977.

[2] M. Sarwar, R. Priestner, J. Mater. Sci. 31 (1996) 2091.

[3] E. Billur, T. Altan, Three generations of advanced high-strength steels for automotive applications, Part I, The first generation, Stamp. J. (2013) (Nov/Dec 2013).

[4] E. Billur, T. Altan, Three generations of advanced high-strength steels for automotive applications, Part II, The second generation, Stamp. J. (2014) (Jan/Feb 2013).

[5] E. Billur, T. Altan, Three generations of advanced high-strength steels for automotive applications, Part III, The third generation, Stamp. J. (2014) (Mar/Apr 2013).

[6] W.F. Hosford, R.M. Caddell, Metal Forming: Mechanics and Metallurgy, 4th edition, Cambridge University Press, 2011.

[7] M.E. Mear, J.W. Hutchinson, Influence of yield surface curvature on flow localization in dilatant plasticity, Mech. Mater. 4 (1985) 395.

[8] V. Tvergaard, Effect of yield surface curvature and void nucleation on plastic flow localization, J. Mech. Phys. Solids 35 (1987) 43.

[9] H.-Y. Jeong, J. Pan, The effects of rate sensitivity and plastic potential surface curvature on plastic flow localization in porous solids, Int. J. Fract. 56 (1992) 317.

[10] K.-C. Liao, J. Pan, S.C. Tang, Approximate yield criteria for anisotropic porous ductile sheet metals, Mech. Mater. 26 (1997) 213.

[11] W.Y. Chien, J. Pan, S.C. Tang, Modified anisotropic Gurson yield criterion for porous ductile sheet metal, J. Eng. Mater. Tech. 123 (2001) 409.

[12] W.Y. Chien, J. Pan, S.C. Tang, A combined necking and shear localization analysis for aluminum sheets under biaxial stretching conditions, Int. J. Plast. 20 (11) (2004) 1953–1981 (ISSN 0749-6419).

[13] J.J. Jonas, Effects of shear band formation on texture development in warm-rolled IF steels, J. Mater. Process. Technol. 117 (3) (2001) 293–299 (ISSN 0924-0136).

[14] Y. Bai, T. Wierzbicki, Int. J. Fract. 161 (2010) 1, http://dx.doi.org/10.1007/s10704-009-9422-8.

[15] A.W. Hudgins, D.K. Matlock, J.G. Speer, C.J. Van Tyne, Predicting instability at die radii in advanced high strength steels, J. Mater. Process. Technol. 210 (5) (2010) 741–750 (ISSN 0924-0136).

[16] Attila Muderrisoglu, Makoto Murata, Mustafa A. Ahmetoglu, Gary Kinzel, Taylan Altan, Bending, flanging, and hemming of aluminum sheet-an experimental study, J. Mater. Process. Technol. 59 (1) (1996) 10–17 (ISSN 0924-0136).

[17] A. Pradeau, S. Thuillier, J.W. Yoon, Prediction of failure in bending of an aluminium sheet alloy, Int. J. Mech. Sci. 119 (2016) 23–35 (ISSN 0020-7403).

[18] N. Le Maoût, S. Thuillier, P.Y. Manach, Aluminum alloy damage evolution for different strain paths – Application to hemming process, Eng. Fract. Mech. 76 (9) (2009) 1202–1214 (ISSN 0013-7944).

[19] K.J. Miller, Metal fatigue—Past, current and future. Proceedings of the institution of mechanical engineers, Part C: J. Mech. Eng. Sci. 205 (5) (1991) 291–304.

[20] K.J. Miller, THE two thresholds OF fatigue behaviour, Fatigue Fract. Eng. Mater. Struct. 16 (9) (1993) 931–939.

[21] P. Efthymiadis, Multiscale experimentation and modeling of fatigue crack development in aluminium alloy 2024, Ph.D. Thesis The University of Sheffield, 2015.

[22] W.S. Rasband, ImageJ, U. S. National Institutes of Health, Bethesda, Maryland, USA, ⟨http://imagej.nih.gov/ij/⟩.

[23] C.A. Schneider, W.S. Rasband, K.W. Eliceiri, NIH Image to ImageJ: 25 years of image analysis, Nat. Methods 9 (2012) 671–675.

[24] M.D. Abramoff, P.J. Magalhaes, S.J. Ram, Image processing with ImageJ, Biophotonics Int. 11 (7) (2004) 36–42.

[25] C. Mesplont, Phase transformations and microstructure-mechanical properties relations in complex phase high strength steels, DEA Science des Matériaux, Université de Lille, 2002.

[26] H. Ghadbeigi, C. Pinna, S. Celotto, J.R. Yates, Local plastic strain evolution in a high strength dual-phase steel, Materials Science and Engineering: A 527 (18), 5026–5032.

[27] H. Ghadbeigi, C. Pinna, S. Celotto, Failure mechanisms in DP600 steel: initiation, evolution and fracture, Materials Science and Engineering: A 588, 420-431.

[28] J. Kadkhodapour, A. Butz, S. Ziaei Rad, S. Schmauder, A micro mechanical study on failure initiation of dual phase steels under tension using single crystal plasticity model, Int. J. Plast. 27 (7) (2011) 1103–1125.

[29] J. Kadkhodapour, A. Butz, S. Ziaei Rad, Mechanisms of void formation during tensile testing in a commercial, dual-phase steel, Acta Mater. 59 (7) (2011) 2575–2588.

[30] P. Marcus, Corrosion Mechanisms in Theory and Practice, 3rd edition, CRC Press, 2012.